MATERIALS SCIENCE

Emergence and inversion of chirality in hierarchical assemblies of CdS nanocrystal fibers

Alexander V. Gonzalez¹, Miranda Gonzalez², Tobias Hanrath¹*

Arranging semiconducting nanocrystals into ordered superstructures is a promising platform to study fundamental light-matter interactions and develop programmable optical metamaterials. We investigated how the geometrical arrangement of CdS nanocrystals in hierarchical assemblies affects chiroptical properties. To create these structures, we controlled the evaporation of a colloidal CdS nanocrystal solution between two parallel plates. We combined in situ microscopy and computational modeling to establish a formation mechanism involving the shear-induced alignment of nanocrystal fibers and the subsequent mechanical relaxation of the stretched fibers to form Raman noodle—type band textures. The high linear anisotropy in these films shares many similarities with cholesteric liquid crystals. The films deposited on top and bottom surfaces exhibit opposite chirality. The mechanistic insights from this study are consequential to enable future advances in the design and fabrication of programmable optical metamaterials for further development of polarization-based optics toward applications in sensing, hyperspectral imaging, and quantum information technology.



Copyright © 2023 Tree
Authors, some
rights reserved;
exclusive licensee
American Association
for the Advancement
of Science. No claim to
original U.S. Government
Works. Distributed
under a Creative
Commons Attribution
NonCommercial
License 4.0 (CC BY-NC).

INTRODUCTION

The emergence of chirality from spontaneous symmetry breaking is a fascinating scientific phenomenon with profound implications spanning all length scales in nature, including spiral galaxies (1), organisms (2, 3), molecules (4), and subatomic particles (5, 6). Optical chirality in inorganic nanostructures has garnered strong interest (7) by virtue of the precisely programmable optical properties of colloidal nanocrystal (NC) building blocks and the ability to direct their assembly into hierarchical superstructures in which constituent components can interact in purposeful and programmable ways (8). In the case of isolated NCs (also commonly referred to as quantum dots or nanoclusters), optical chirality can arise from interactions between the inorganic particle core and the surrounding organic ligand shell (9-11). However, even NCs that are achiral by themselves can exhibit emergent chiroptical properties in an ensemble due to asymmetries of the electron density in the highly polarizable inorganic core. In some instances, bottom-up assemblies of one-dimensional (1D) nanomaterials have exhibited strong interactions with chiral light due to the emergence of their mesoscopic anisotropic architecture (12, 13). A review by Kotov and coworkers categorized multiple sources of chirality in nanoparticle assemblies and described the scientific quest to understand the relative contributions to emergent chirality as both complex and fascinating (14).

Self-organization in nonequilibrium soft matter systems presents intriguing scientific questions with profound technological impact. For example, recent advances in the directed assembly of NC building blocks into highly ordered superstructures have opened a rich opportunity to explore programmable chiroptical metamaterials with chirality amplification and achieve large dissymmetry metrics (the dimensionless Kuhn factor, also known as the *g* factor) (15). Hierarchical NC assemblies are exciting as they allow scientists to examine how chirality amplification emerges from symmetry breaking and how the chirality is transmitted

across multiple length scales. From a technological perspective, fabricating these materials via inexpensive and scalable solution-based processes has important implications for chiroptical metamaterials (16) in applications ranging from sensing (17, 18) to catalysis (19) to emerging quantum computing (20, 21).

Evaporation-driven self-assembly in confined geometries, particularly the quasi-2D confinement between two parallel plates (i. e., Hele-Shaw cell), provides an advantageous experimental platform for several key reasons: (i) The kinetics of drying and the concentration field of the solute can be rigorously controlled and quantitatively described with analytical models, and (ii) the dynamics of the receding liquid meniscus can be easily observed with video and microscopy imaging (22, 23). We previously showed that controlled evaporation in a confined geometry enables the formation of highly uniform hierarchical superstructures in which CdS NCs (i.e., 2-nm magic-sized clusters also commonly referred to as quantum dots) (24) are arranged into 2-µm bands, which are uniform across the 2-cm scale film (25). These hierarchical NC assemblies share many structural and optical characteristics with liquid crystals (LCs) (26-30). For example, analysis of the NC fiber pattern formation from the perspective of a quasi-cholesteric LC provides valuable guidance to understand the mechanism for the higher structure and the relation to emergent chiroptical properties. Whereas in conventional NC assemblies, the dichroic effects are adversely affected by strong scattering (31), the relatively small CdS clusters explored in this study scatter light more weakly and thus enable pronounced chiroptical response as quantified by the g factor as shown below.

Yao et al. (32) recently reported that hierarchical NC fiber assemblies exhibit strong chiroptical properties with circular dichroism (CD) g factor as high as 0.05; however, how the emergent chiroptical properties relate to the hierarchical NC film structure and how the structure in turn emerges during the assembly have remained unclear. Moreover, whether the large anisotropic lightmatter interaction arises from mesoscopic structure effects or the chirality of basic NC building blocks is currently not well understood. Accordingly, this study focuses on understanding the

¹Robert F. Smith School of Chemical and Biomolecular Engineering, Cornell University, Ithaca, NY 14853, USA. ²Department of Materials Science, Arizona State University, Tempe, AZ 85281, USA.

^{*}Corresponding author. Email: tobias.hanrath@cornell.edu

underlying processing-structure-property relationship and applying that knowledge to establish design principles for NC assemblies as programmable hierarchical chiroptical metamaterials.

A key discovery of the present study is that the NC films formed on the top and bottom surface absorb circularly polarized light in selectively opposite quantities (i.e., top and bottom films always show opposite chirality, although the specific chirality on either the top or bottom film is stochastic) (Fig. 1). This discovery leads to two key questions that we aim to address in this paper: (i) what is the fundamental relationship between the chiroptical properties and the structure of this soft-matter thin film and (ii) what is the mechanism underlying the chirality inversion between the top and bottom films? To address these questions, we introduce a mechanism that correlates chirality inversion and transmission to the interplay of hydrodynamic and physicochemical subprocesses, including the shear-induced alignment of NC fibers in the receding meniscus and the spiral propagation of a mechanical undulation in the thin film. The mechanistic insights from this study are consequential to enable future advances in the design and fabrication of programmable optical metamaterials, particularly for methods that combine molecular self-assembly and additive manufacturing techniques (33).

RESULTS AND DISCUSSION

We formed the hierarchically ordered NC assemblies by evaporating a colloidal NC suspension (20 mg/ml in hexane) confined between two parallel glass slides to define a circular droplet of radius (~5 mm) and height defined by a spacer with height, H (typically 50 to 300 μ m) (Fig. 1A). The basic building blocks for this assembly are 2-nm magic-sized (i.e., $Cd_{37}S_{18}$) NCs, which are passivated with a ~1.8-nm-thick oleate ligand shell. After the solvent completely evaporated, we separated the top and bottom films to analyze the NC film structure and optical properties.

We examined the microstructure of the NC film with a combination of atomic force microscopy (AFM), scanning electron microscopy (SEM), and laser scanning confocal microscopy (LSCM) (see "Structure analysis of the hierarchical assemblies of helical NC fibers" section in the Supplementary Materials). The mesoscale structure of the NC films is characterized by the hierarchical arrangement of ~2-nm NCs into fibers, which, in turn, arrange to form ~2-µm-wide bands (Fig. 1B). We discuss the film formation mechanism and structure in detail below. Although the fundamental base unit (i.e., the Cd₃₇S₁₈ NC) is quasi-spherical, the similar size of the surface-bound oleate ligand shell and the inorganic NC core give rise to a mesophase behavior that is characterized by the formation of fibers as illustrated in Fig. 1B and detailed in our previous work (25, 34). The complex directional anisotropies spanning multiple length scales have important implications on light-matter interactions and emergent chiroptical properties that may be governed by the simultaneous influence of linear and CD and birefringence.

The CD spectra in Fig. 1C show that the NC films deposited on top and bottom surfaces exhibit opposite chirality. To understand how the symmetry breaking and emergent chirality relates to the linearly anisotropic mesoscale structure of the NC film, we need to consider the relative contributions of CD, circular birefringence, linear dichroism (LD), and linear birefringence (LB). To a first approximation, the magnitude of the LDLB contribution can be

examined by flipping the sample around the vertical axis (i.e., changing the direction of the optical beam traversing through the sample). In cases where the LDLB dominates over CD, the sign of the measured CD is inverted when the sample is flipped. For example, this polarity inversion of ellipticity has been reported in thin films of π -conjugated materials with pronounced linear anisotropies (35). Notably, CD spectra of the NC films shown in Fig. 1C do not show a sign reversal upon flipping the sample. However, the detailed shape of the bisignate CD signature is influenced by the direction of the optical beam through the sample. The magnitude of LDLB contributions can be approximated by the methods reported by di Bari et al. (35), which was also recently extended to NC fiber films as reported by Yao et al. (32). To interpret how LD and LB contribute to the CD spectra, we performed four orientationally independent CD scans on a sample site, including two scans around the optical beam path to correct for instrumental artifacts and two scans of a film facing toward and away from the beam path (Fig. 1C). We provide additional details on the analysis to decouple apparent CD, determining LDLB effects, and a summary of samples' chiroptical properties in the Supplementary Materials ("Additional discussion on chirality transmission" section in the Supplementary Materials and table S1). On the basis of this "four-scan analysis," we can approximate the ratio of the LDLB to intrinsic CD signature to $\sim 0.19 \pm 0.1$ (n = 16 samples), which suggests that the LDLB contribution is notable but not dominant.

Whereas the four-scan analysis provides an initial estimate of the LDLB contribution to the CD spectrum, there are many interrelations between the elements of the Mueller matrix, which complicate the analysis, as noted by Hovenier (36). One complication is that four-scan analysis described above assumes that the structural anisotropies are homogeneous in the direction of light propagation. For inhomogeneous layers with cholesteric twisted structure, there remains a contribution to the CD stemming from the combination of dichroism and birefringence, which cannot be separated out by flipping the sample. Whereas the structure analysis detailed below shows that the NC films are anisotropic yet homogeneous in the lateral direction (i.e., in the *x,y* plane), the homogeneity of the film structure in the vertical direction is currently not well understood. We will return to the topic of the heterogeneity of the NC film in the structure analysis below.

Considering the multiscale directional anisotropies illustrated in Fig. 1B, we sought to understand whether chirality emerges at the level of NC fibers or whether it emerges as the result of higher-order structures in the film. Because the optical properties of the magicsized CdS NCs are sensitive to the molecular configuration of the surrounding ligand shell (24), we considered how chirality could be transmitted from the micrometer-scale bands to the nanometer-scale NCs (fig. S21). Because the hierarchical films can exhibit local symmetry breaking (i.e., helical pitch of individual fibers) and global symmetry breaking (e.g., geometric arrangement of proximate fibers within the film), we sought to decouple the contributions of nanoscale and microscale structures on the emergent chirality. We performed a control experiment in which we disrupted the higher-order structure of the film and formed an isotropic mixture of the fibers in KBr powder. Our previous work on the fibers suggests that the fibers are robust and stabilized by the mesophase behavior (25, 34). Accordingly, the local ordering (e.g., helical pitch) of isolated fibers is preserved whereas the global ordering is disrupted. The KBr experiments (fig. S6) show that the

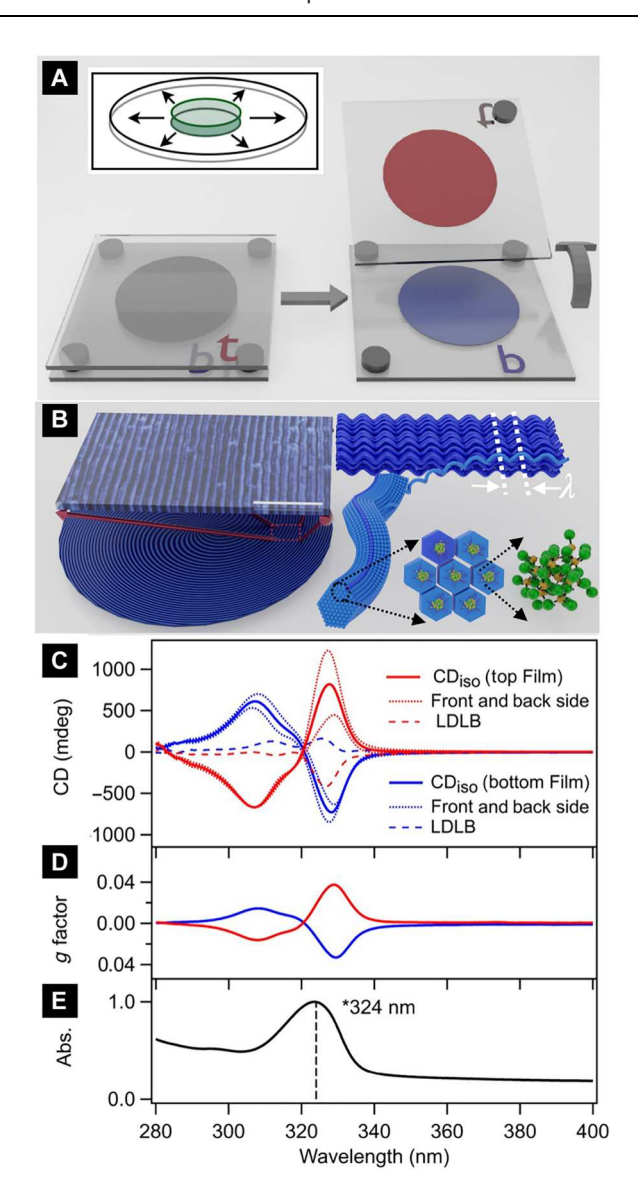


Fig. 1. Symmetry breaking in thin films of hierarchically self-assembled CdS NCs. (A) Schematic illustration of the experiment in which controlled evaporation of a colloidal NC suspension constrained between two parallel plates leads to the formation of thin films with opposite chirality on top (red) and bottom (blue) substrates. (B) Illustration of the hierarchical structure of the "Raman noodle"–like NC fiber assembly, including magnified views of an isolated fiber and the atomic structure of the magic-sized $Cd_{37}S_{18}$ NC, surface-bound oleic acid ligands is omitted for clarity. Spectra of (C) CD and LDLB. The two mesh lines for top and bottom substrates indicate front and back scans to correct for LDLB contributions, where each meshed line corresponds to the averaged 0° and 90° orientations around the beam path. The dashed lines correspond to LDLB contributions, determined via extracting the orientationally averaged CD spectra (solid lines). (D) Corresponding spectrum of the *g* factor and (E) normalized optical absorption of the NC films shows the excitonic peak at 324 nm.

CD nearly vanished, and the *g* factor of isolated NC fibers in a KBr pellet is orders of magnitude smaller than the hierarchically ordered film. We interpret the absence of CD in the isotropic NC fiber powder as an indication that the optical chirality does not arise from the structure of isolated fibers. Instead, this control experiment suggests that the observed chirality emerges due to the

higher-order linear arrangement of fibers within the film at the mesoscopic level. We argue that the key to explaining and ultimately controlling the emergent chiroexcitonic properties (including the inversion and multiscale transfer) lies in understanding how the NC fibers evolve from the colloidal suspension to the highly ordered hierarchical superstructures. Accordingly, we set out to understand the mechanism by which the hierarchical NC structures form, as detailed below.

In situ microscopy analysis provides critical insights into the evolution of the hierarchical NC film structure during the evaporation-driven assembly as summarized in Fig. 2. We monitored the evolution of the NC film structure in real time using in situ LSCM and provide a video of the receding liquid meniscus and the subsequent emergence of the banded texture in the drying film in the supplementary materials. Figure 2A provides LCSM snapshots at the 3 o'clock position of the film (i.e., the green region, $\theta = 90^{\circ}$, shown in the top left inset); these images illustrate the emergence of undulated bands as the remaining solvent in the wet film evaporates. The overall NC film thickness (z) is in the range of 1 and 6 µm and can be tailored by adjusting the gap height (i.e., the total volume of the NC suspension for a constant droplet radius, R_0) or the concentration of the colloidal NC suspension (see fig. S7). Because the NC film thickness, z, is approximately an order of magnitude larger than the amplitude of the undulation, we conclude that the NC film is continuous, which is important because it shows that the formation mechanism is distinct from similar coffee-ring deposits formed by stick-and-slip mechanism in which case the film thickness vanishes in between the deposited rings (37). Higher-resolution SEM (Fig. 2B) and AFM (Fig. 2C) images reveal the detailed sinusoidal structure of the bands with a "torsade" orientation of the constituent helical NC fibers with an average diameter of 300 nm (Fig. 2C and figs. S8 and S9).

The proposed mechanism responsible for the emergent pattern in the NC fiber film is illustrated in Fig. 2D. The formation of the banded texture involves the interplay of physicochemical and hydrodynamic processes. The evaporation of the solvent increases the NC solute concentration, which leads to the mesophase transformation of NC fibers as described in our earlier work (25, 34). Forcing the phase boundary (of the isotropic-to-nematic transition) to travel by mechanical displacement of the fluid meniscus has important implications on the formation of nonequilibrium states characterized by the long spatial correlation of the director phase (38). Analogous to previous reports of nematic LCs (26-29), the pattern formation can be described as a two-step sequence involving (i) the shear-flow alignment (39, 40) of NC fibers (Fig. 2E) and (ii) the subsequent mechanical relaxation of the stretched fibers results in buckling or undulation of the film (Fig. 2F). We analyzed the intensity profile of the LSCM image and the transformation from initial undulation modes and final equilibrium bands with wavelength λ (Fig. 2, G and H). Because the meniscus recedes at a rate of about 1.7 µm/s, we can capture the evolution of the band texture in both the temporal and spatial reference frames. We provide additional discussion of the propagation mode of the mechanical relaxation in the supplementary materials (see "Analysis of the velocity of the receding meniscus" section in the Supplementary Materials). As we will discuss in more detail below, how the pattern formation is triggered has important implications on the symmetry breaking responsible for the formation of inverted chiroptical films on the top and bottom surface.

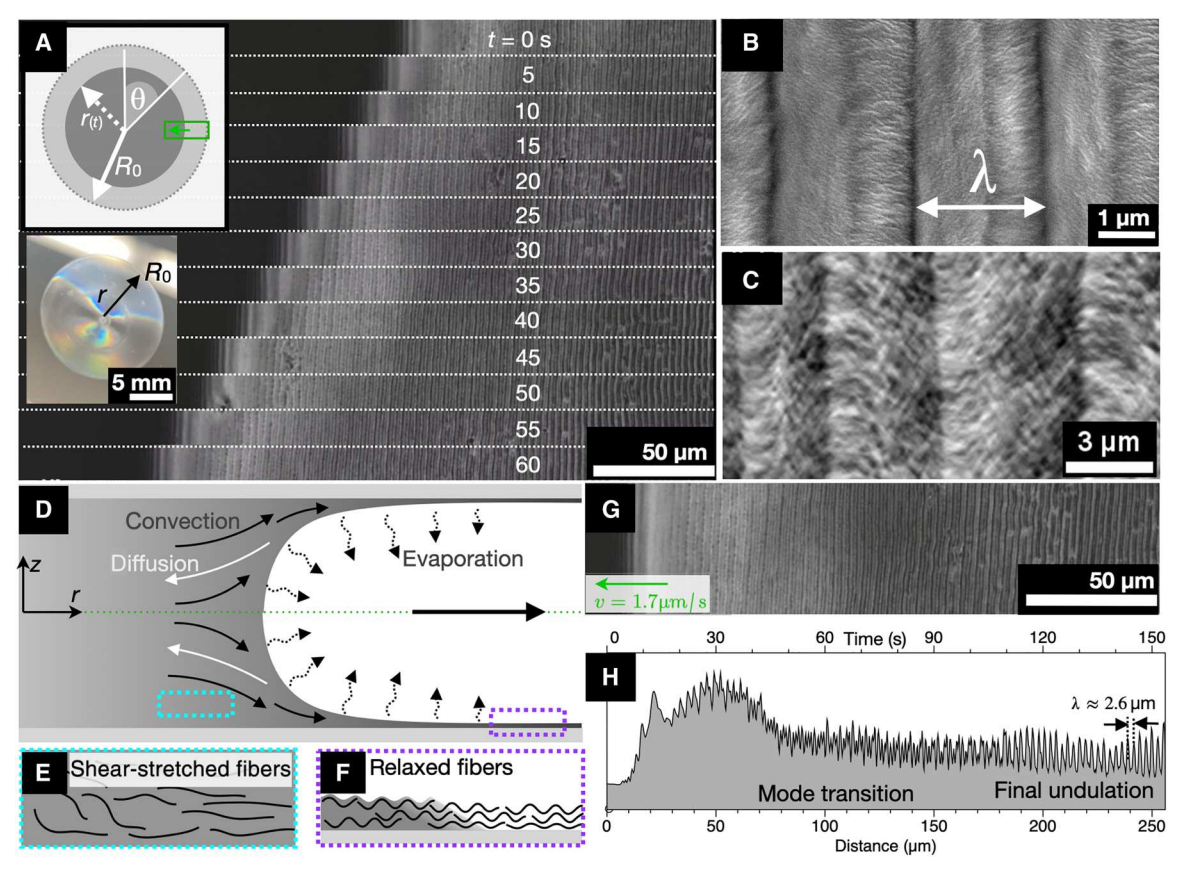


Fig. 2. Evolution of the NC film structure during evaporation driven assembly. (**A**) Video snapshots of the green region (at $\theta = 90^{\circ}$) in the inset show the right-to-left receding liquid meniscus and the emergence of band textures in the deposited film. The featureless dark region on the left is the isotropic liquid and right side shows the periodically forced phase winding with a large coherence length perpendicular to the interface. (**B**) High-resolution SEM image and (**C**) superimposed AFM topography images, scanned at 0° and 90° relative to the band axis, showing the fine torsade structure of bands emerging from the undulation of constituent fibers. (**D**) Side-view illustration of the receding meniscus and corresponding magnified perspectives illustrating the sequential (**E**) shear-induced alignment of fibers and (**F**) subsequent relaxation leading to the formation of periodic band texture undulations. (**G**) Higher-magnification image and (**H**) corresponding intensity profile of the band texture illustrating the initial growth modes, transition region and final undulations with a ~2.6-μm wavelength. On the basis of the meniscus receding at a rate of about 1.7 μm/s, this analysis panel illustrates both the temporal (top axis) and spatial (bottom axis) evolution of the film

Having established the mechanism responsible for the formation of the banded NC thin film texture, we now turn our attention to examining how key structure parameters (i.e., wavelength, amplitude and long-range coherence of the undulations) are affected by processing conditions. We analyzed LSCM images to quantify how the wavelength (λ) and amplitude (A) of the NC film structure change along the radial position within the film. Analysis of the LCSM images in Fig. 3A reveals that the band wavelength (λ) increases toward the center of the circular film (i.e., $r/R_0 = \rho \rightarrow 0$), whereas the corresponding amplitude decreases (Fig. 3B). The radial variation in wavelength and amplitude are consistent for experiments with varying gap heights, H = 50, 100, and 300 µm. We adjusted the volume of the deposited NC suspension (20 mg of NC/ ml of hexane) to maintain consistent droplet area ($R_0 = 6 \pm 1 \text{ mm}$) for all experiments. The counteracting trends in λ and A can be conveniently summarized via the dimensionless wave number ($\kappa =$ $2\pi A/\lambda$), which monotonically decreases toward the center of the film (Fig. 3C). We will return to wave number, k below as a convenient metric for the pitch of the twisted fibers to correlate the hierarchical structure and the emergent chiroptical properties (41, 42). We examined the long-range spatial coherence of the band undulations based on Fourier transform analysis of the microscopy images. This analysis revealed that the spatial coherence and uniformity of the band undulations decrease toward the center of the film.

To explain the observed trends in wave number (κ) and spatial coherence of the band undulation with radial position within the film, we need to consider the dynamic interplay between the physicochemical and hydrodynamic processes. At first glance, the formation of the NC film shares several similarities with liquid film coating processes (37). However, given that the colloidal NC suspension is a relatively complex fluid, additional factors, particularly the coupled dynamics of the mesophase transformation (34), the solvent evaporation, the mechanical relaxation of the fibers (27), and ultimately the drying of the film, require careful consideration to explain the relationship between κ and ρ .

The well-defined evaporation conditions prevailing in the Hele-Shaw cell (i.e., circular droplet of NC suspension confined between two parallel plates) allow the evaporation dynamics and spatiotemporal NC concentration profiles to be captured by analytical models (23). A basic mass balance and validating control experiments show that the velocity of the receding meniscus is approximately constant (fig. S11). We adopted the model described by Salmon and

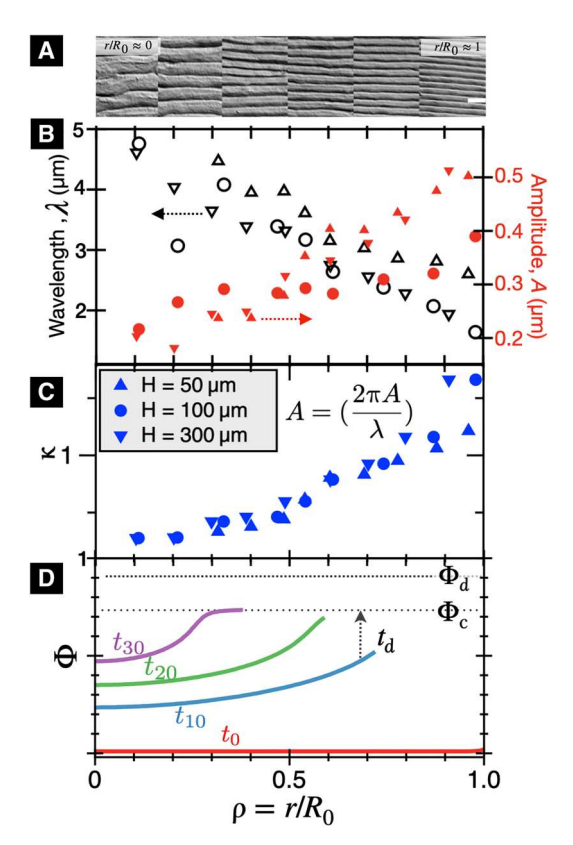


Fig. 3. The evolution of the NC fiber film structure as a function of reduced radius r/R_0 of the film. (A) A series of LCSM images of NC film at varying radial positions. (B and C) Corresponding wavelength, λ , and amplitude, A, as well as the wave number $\kappa = 2 \pi A/\lambda$ of the undulations for a series of experiments with gap heights H=50, 100, and 300 μ m. (D) Analytical model of the spatial and temporal evolution of NC concentration during the film formation.

coworkers (22) based on basic transport equations for the binary (i. e., NC and solvent) mixture to describe the spatiotemporal evolution of the NC concentration $(\Phi_{(r,t)})$ during film formation (see "Concentration field model in drying droplet" section in the Supplementary Materials). The competing dynamics of the receding fluid meniscus and the NC diffusion within the remaining liquid are conveniently parametrized by the dimensionless Péclet number. In the case of a circular droplet confined between parallel plates, this can be described as: Pe = $R_0^2/D_0\tau_D$. If the distance the NCs can explore by diffusion is larger than the droplet area (i.e., Pe < 1), then the NC concentration (Φ) within the liquid remains relatively homogeneous in space but increases gradually with time as the solvent evaporates. Conversely, if Pe > 1, then appreciable NC concentration gradients build up near the edge of the receding meniscus. As detailed in the Supplementary Materials [and (21)], the prevailing diffusion characteristics can be obtained from literature and also conveniently extracted from experimental fits to the temporal evolution of the droplet area $(\alpha_{(t)} = A_{(t)}/A_0)$. On the basis of this analysis, our NC assemblies were formed under conditions parametrized by Pe \approx 0.6 and an initial NC concentration of Φ = 0.01, which is intermediate to the two regimes described above. Key trends of the NC concentration profile $(\Phi_{(r,t)})$ derived from this model are summarized in Fig. 3D.

The spatiotemporal evolution of the NC concentration $(\Phi_{(r,t)})$ shown in Fig. 3D shows that both the overall NC concentration and the concentration polarization (i.e., concentration gradient from the center of the droplet toward the meniscus) increase with time. Combined with the fact that the contact line velocity (and by extension the deposition rate) is approximately constant, these trends suggest that the film thickness should increase toward the center of the droplet. This trend is corroborated by experimental measurements of the film thickness shown in fig. S7. The observation that the wavelength of the undulation increases toward the center of the film can therefore be explained on the basis of linear mechanical instability analysis of wrinkles formed in thin films (43), which predicts that the undulation wavelength scales with the thickness of the film.

To understand why the spatial coherence of the band undulations decreases toward the center of the film, we need to consider the competing dynamics of solvent evaporation and the formation of the bands. The structure of the liquid film transforms from a dilute suspension of NC fibers to a condensed assembly. To describe the formation of the fibrous mesophase and the subsequent complete drying of the film (Fig. 2G) in context of the spatiotemporal NC fiber concentration gradients (Fig. 3D), we considered two concentration thresholds. For simplicity, we considered $\Phi_c \approx 0.74$ and $\Phi_{\rm d} \approx 0.9$ as the close packing fractions of spheres and cylinders, respectively. While the droplet shrinks, the time to evaporate the remaining solvent (from the bulk suspension and from interstitial volume between the NC fibers) decreases (see t_d in Fig. 3D). In other words, the deposited fibers have progressively less time to respond to the mechanical stresses and configure into their equilibrium undulation wavelength as the liquid meniscus proceeds to the center of the circular deposit. To further corroborate this interpretation, we provide additional analysis (fig. S14) to show that the long-range spatial coherence of the band structure is directly proportional to the wave number, suggesting that fibers in initially formed film (i.e., $\rho \rightarrow 1$) have more time to assemble into a coherent superstructure.

We now turn to describe how the emergent chiroptical properties relate to the NC assembly structure. The combination of sizemonodisperse (i.e., magic-sized) NCs with a sharp excitonic absorption spectrum (34) and high-fidelity assembly (i.e., welldefined periodicity with long-range ordering) affords an advantageous experimental platform to examine the foundational structure-property relationship and elucidate the mechanism underlying the emergent chirality. Figure 4A summarizes the trends in g factor as a function of topographical wave number. The general trend is that the optical anisotropy increases exponentially with increasing wave number. In other words, the largest g factors are observed near the edge of the dry film. Near the upper bound of currently accessible κ values, the measured g factors (based on averaging the apparent CD at four orientationally independent scans to account for LDLB, as detailed above) are in the range of 0.06; this is among the highest reported g values among semiconducting NCs (see sample structure-property analysis summary in table S2).

Beyond establishing the general relationship between wave number and g factor, we note that the variation of rotator strength evident in Fig. 4A points toward additional complexities in the structure-property relationship that are not captured in the basic model. For example, the three samples with $\kappa \approx 2$ exhibit g

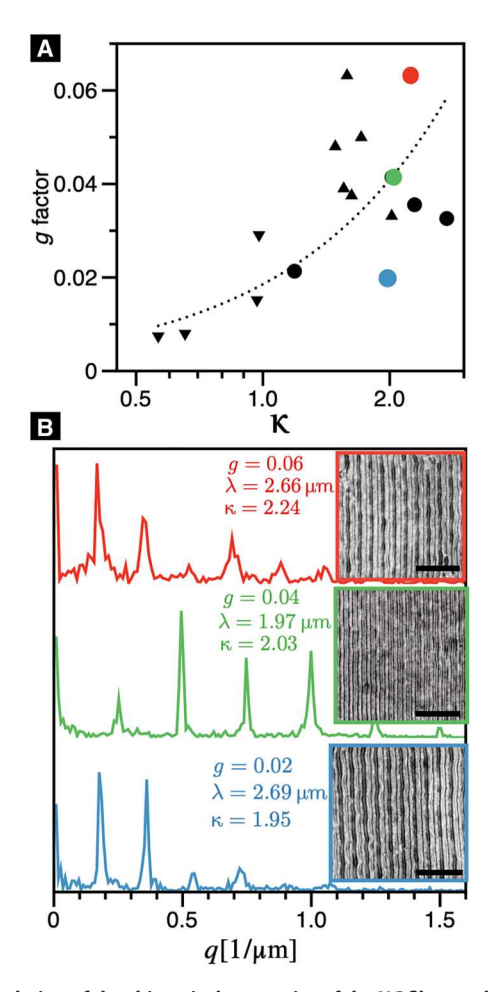


Fig. 4. Correlation of the chiroptical properties of the NC films to the λ/A band texture structure parameter. (A) Relationship between g factor and structure. The dashed line is an exponential fit to the experimental data. (B) Fourier transform magnitude versus wave vector (q) for three select samples with similar wave number, κ and corresponding LSCM images. Scale bar, 20 μ m.

factors ranging from 0.020 to 0.063, which suggests that the wave number is necessary but insufficient to describe how the NC film structure affects emergent chiroptical properties. To explain these second order contributions, we hypothesized several structural inhomogeneities that affect the interrelations between the elements of the Mueller matrix.

One possible contribution to structural inhomogeneity is the long-range spatial coherence of the band texture, which relates to the rotator strength based on dipole coupling theory (44). However, whereas the wave number is correlated to the long-range order within a given sample (fig. S14), the Fourier transform analysis of the corresponding microscopy images in Fig. 4B does not reveal any clear relationship between the *g* factor and the spatial coherence (i.e., the width of the wave vectors). The ordering of softmatter assemblies can be improved by solvent vapor annealing; however, experiments detailed in the Supplementary Materials (fig. S17) show that solvent vapor annealing only marginally improves the NC fiber assembly structure and associated *g* factor.

A closer inspection of both the images and the corresponding distribution of wave vectors suggests an additional fine structure in the band texture (q=0.2 and q=0.45). The sample with the distinct fine-structure (i.e., additional groves) pattern also shows a distinct line shape in the CD spectrum (fig. S3 to S5). We note an interesting parallel to the chiroptical properties of proteins, for which the detailed line shape of the CD spectrum is sensitive to the secondary structure of the folded protein (45). We expect that similar secondary structure effects in the NC fiber films (25) may also be operative here; establishing the impact of primary and secondary structure on the CD line shape is the subject of future computational and experimental studies.

We examined how the mesoscale structure may vary along the path of the optical beam traversing through the sample (i.e., the z axis). Specifically, variations of the band undulation amplitude along the z axis may introduce interrelations between elements in the Mueller matrix. For example, fibers deposited near the solid substrate surface are subject to different boundary conditions than fibers near the solution/air interface (Fig. 5A). Specifically,

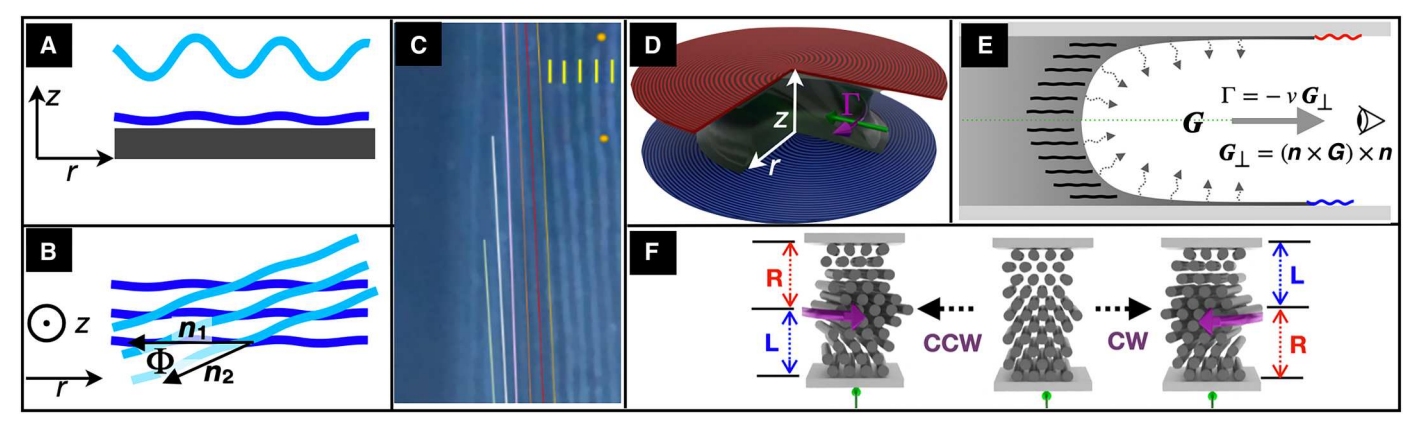


Fig. 5. Chirality inversion. Schematic illustration of structural heterogeneities in the NC film, including (**A**) variation in the NC fiber undulation amplitude as a function of film thickness, and (**B**) misalignment of the NC fiber director. (**C**) In situ microscopy video snapshot demonstrating the nonzero angle offset between the receding meniscus and the spiral propagation of bands. (**D**) Proposed mechanism for chirality inversion based on shear (green) and torsional (purple) force. During the formation of the film, shear forces from the receding meniscus align the filaments toward the center of the circle. The mechanical instability responsible for the undulating band texture propagates in a spiral direction. (**E**) Model of the chemical Lehmann effect coupling between the chemical potential gradient (*G*, defined by the vapor pressure profile) and the director (*n*) of the cholesteric NC fiber. (**F**) Illustration of the chirality inversion resulting from clockwise or counter-clockwise propagation.

because of the adhesion of fibers to the solid substrate surface, we expect the amplitude of the band undulation to gradually increase going from the substrate interface to the free surface. To test this interpretation, we examined vertical variations in the band undulation amplitude by examining LSCM images acquired at varying focal depths through the z axis of the film. This analysis revealed inhomogeneous stacking layers of the NC fibers, from an undulated topography to a softened film at the film-substrate interface (movie S2), which suggests that variations in the undulation amplitude are likely but cannot be adequately quantified and correlated to the chiroptical properties. Moreover, this variation would be symmetric on both top and bottom NC films, and this does not explain the observed chirality inversion.

Even subtle variations in the macroscopic radial alignment of NC fibers within the film (Fig. 5B) can have a notable effect the emergent chiroptical properties. The shear-induced alignment orients the major axis of the NC fibers toward the center of the radial droplet, and the undulation bands are oriented orthogonally to the NC fiber axis (Fig. 5B). In this basic model, all NC fibers are oriented radially inward. However, careful inspection of the in situ microscopy video reveals that the propagation of the band proceeds with a small but notable nonzero angular offset. This ostensibly small deviation has important implications not only for the mesostructure of the NC film but also for the mechanism responsible for the symmetry breaking because it suggests that the bands are formed in a spiral rather than concentric form.

A mesoscale structure in which the director of the NC fiber varies along the z axis of the film (see Fig. 5B) presents interesting analogies to Bouligand structures. For example, Pauly and coworkers (13) recently showed that Bouligand structures prepared by bottom-up manufacturing through layer-by-layer assembly of plasmonic nanowires gave rise to a large chiroptical response with an ensemble of dichroic and birefringence effects. Their analysis of the underlying structure-property relations used Mueller matrix polarimetry to show that the CD is due to the chiral superstructure and also noted that the sign of the CD signal does not flip upon rotating the sample. A detailed quantification of the relative contribution of the three structural heterogeneities outlined above is not yet possible. However, we emphasize that the third heterogeneity (i.e., variation in the alignment of the NC fiber director) (i) is corroborated by evidence from the in situ microscopy video, (ii) explains the high dissymmetry factors as a quasi-Bouligand chiroptical metamaterial, and (iii) provides a critical clue to explain the symmetry breaking between top and bottom surfaces as detailed below.

Whereas the preceding discussion describes the foundational mechanism by which the hierarchical NC film structure evolves and how the structure relates to emergent chiroptical properties, we lastly return to the outstanding question: Why do the films deposited on the top and bottom surfaces exhibit opposite chirality? We argue that the chirality inversion is a direct result of hydrodynamic forces acting on the fibers during the early stages of film formation. At the onset, it is important to recognize that symmetry breaking must occur at a stage in the film formation when the top and bottom films can "communicate." Chung *et al.* (*37*) previously reported that a liquid crystalline film of M13 phage virus shows opposite mesoscopic chirality between the left and the right side of the substrate, regardless of the inherent molecular chirality. The authors claim that the spatial chiral inversion is due to hydrodynamic interactions led by opposing meniscus forces. In the language of the

mechanism introduced in Fig. 2, this constraint suggests that the chirality inversion is mediated through the liquid meniscus connecting the two substrates.

To understand why the orientation of the major axis of the NC fibers may vary with vertical position within the film, we need to consider the detailed forces acting on the fiber during the assembly. We interpret the nonzero offset between the geometric radial and the band (see figs. S19 and S20) as indicating a torsional force acting on the NC fiber during the assembly (Fig. 5C). Whereas the shear forces associated with the receding meniscus have already been discussed above, the origin of the torsional force is less obvious. We propose that the torsional force arises from the coupling between the director (n) of the NC fiber and the chemical potential gradient (G, associated with the radial gradient of the solvent vapor pressure). An analogous "chemical Lehmann" effect was previously observed for monolayers of an LC in a Langmuir trough and analyzed by theoretical models describing the pattern formation and the initial nucleation (46). Tsori and DeGennnes (47) showed that the nucleation of this effect is related to relaxation of internal elastic energy associated with frustrations from anchoring the director at lateral boundaries. The formation of periodic patterns is thus attributed to the repeated formation of disclinations that move away from each other. Although the specific geometry of a circular meniscus confined between two parallel plates presents different boundary conditions and topology from the planar configuration described in earlier models. We provide additional discussion of the chemical Lehmann effect in the "Inversion of chirality based on chemical Lehmann effect" section of the Supplementary Materials. We argue that the general physical phenomenon holds to describe the origin of the torsional force responsible for the spiral propagation of the banded undulation.

In summary, we established the foundational processing-structure-property relationships of hierarchical assemblies of CdS NC fibers. We combined experiments and modeling to understand the mechanism responsible for forming hierarchical superstructures and how the structure affects the transmission of chirality across many length scales. We interpret the symmetry breaking underlying the formation of mesostructured films to a chemical Lehmann effect based on the coupling between the director of the NC fiber and a chemical potential gradient.

Looking forward, we note that the ability to tailor the hierarchical architecture of the fiber assemblies has profound scientific and technological implications. We see that technological implications. We see the emergence of opposite chirality in evaporation-driven assembly between two parallel plates as an exciting advance toward the programmable formation of chiroptical metamaterials. Moreover, we hope that the mechanistic insights from the model discussed above and the relatively simple experimental implementation of this method will spur future advances. We see compelling prospects to leverage control over local hydrodynamic conditions as a promising design principle to engineer more complex (i.e., macroscopically patterned) chiroptical films. For example, functionalizing the substrate to engineer patterns in local contact angles (48) or incorporating pillar structures within the parallel plate opens intriguing prospects to leverage local variations in hydrodynamic shear to design, fabricate, and study bioinspired chiroptical metamaterials (49).

MATERIALS AND METHODS

Materials

Cadmium oxide powder (CdO, 99.5%), oleic acid ($C_{18}H_{34}O_2$, 90%), sulfur powder (S, reagent grade), and trioctylphosphine (97%) were purchased from Sigma-Aldrich. Hexanes (95% anhydrous) were used as a solvent for all prepared solutions. All chemicals were used as manufactured, without any further modifications.

Solventless synthesis of high-purity CdS "magic-sized" nanoclusters

Monodisperse cadmium sulfide "magic size clusters" were synthesized according to previously described methods by Nevers et al. (34).

Thin film preparation

Transparent CdS nanocrystals solutions were prepared with hexanes solvent at a concentration of 20 mg/ml in a 3-ml vial. The solution was placed on a stir plate at 400 rpm for at least 12 hours. (Note that freshly synthesized nanocrystals result in colorless and transparent solutions. A cloudy solution indicates degradation of the nanoparticle mesophase.) Glass substrates (1.0 to 1.2 mm in thickness) were cut into 25 mm–by–25 mm squares and plasmacleaned at 38 W for 5 min. Before drop-casting the MSC solution, spacers (double sided tape $\sim\!100~\mu\mathrm{m}$ or heavy-duty tin foil $\sim\!25~\mu\mathrm{m}$ in thickness) were positioned in a "U" shape around the perimeter of the substrate surface. CdS NP solutions were then drop-casted in the center of the, now modified, substrate, and a glass cover slip was placed promptly on top to contain the solution.

Optical property analysis

A Jasco J-1500 CD spectrometer concurrently measured the CD, LD, and absorption spectra of MSC thin films. We scanned samples at room temperature at a wavelength range of 280 to 400 nm, a data pitch of 0.2 nm, a bandwidth of 1.0 nm, and a scanning speed of 50 nm/min. A glass baseline measurement for each experiment was collected and subtracted from the thin film spectra. To ensure that optical data corresponded to the thin film structure, we fixed a 2.5-mm-diameter aperture in the beam path and marked the bounds of the measurement site on the sample. All measurement sites were scanned front and back at orientations of 0° and 90° and averaged to extract the orientationally averaged CD.

Structural property analysis

A Keyence VK-X260 3D Laser Scanning Confocal Microscope was used to probe the structure of thin film samples. The laser profilometer was operated in surface profile mode, with an aspect ratio set to 2048×1536 pixels, and a z-pitch resolution of 180 nm. Thin films' thickness and topography profile were measured in the Multi-file Analysis Application VK-H1XME. Images acquired with the LSCM were analyzed with FFT in ImageJ to determine the periodicity.

Thin films topography and phase contrast information were obtained via AFM (Asylum-MFP3D-Bio-AFM-SPM). Thin film surfaces were scanned with a standard Olympus AC160TS-R3 probe in tapping (ac) mode at room temperature. Acquired AFM images were analyzed in Igor.

A Zeiss Gemini 500 Scanning Electron Microscope was used to probe the topography of thin film surface. For sample preparation, glass substrates were secured at each corner with conductive carbon tape, silver paint was generously distributed on the glass substrate (without touching the thin film), and a strip of copper tape linked the thin film to the bottom of the sample holder. Next, samples were coated with gold and palladium before being placed in the SEM vacuum chamber.

Supplementary Materials

This PDF file includes:

Supplementary Text Figs. S1 to S21 Tables S1 to S3 Legends for movies S1 to S3 References

Other Supplementary Material for this manuscript includes the following:

Movies S1 to S3

REFERENCES AND NOTES

- S. V. Chervon, Chiral cosmological models: Dark sector fields description. Quantum Matter 2, 71–82 (2013).
- H. R. Gelderblom, Structure and classification of viruses, In Medical Microbiology, S. Baron, Ed. (University of Texas Medical, ed. 4,1996), chap. 41.
- W. Jiang, X. Yi, M. D. McKee, Chiral biomineralized structures and their biomimetic synthesis. *Mater. Horiz.* 6. 1974–1990 (2019).
- 4. F. Devínsky, Chirality and the origin of life. Symmetry 13, 2277 (2021).
- S.-F. Ge, P. Pasquini, Parity violation and chiral oscillation of cosmological relic neutrinos. *Phys. Lett. B* 811, 135961 (2020).
- 6. Only left-handed particles decay. Nature 524, 8 (2015).
- A. Visheratina, N. A. Kotov, Inorganic nanostructures with strong chiroptical activity. CCS Chemistry 2, 583–604 (2020).
- X. Lan, Z. Su, Y. Zhou, T. Meyer, Y. Ke, Q. Wang, W. Chiu, N. Liu, S. Zou, H. Yan, Y. Liu, Programmable supra-assembly of a DNA surface adapter for tunable chiral directional self-assembly of gold nanorods. *Angew. Chem. Int. Ed.* 56, 14632–14636 (2017).
- H. Yoshida, M. Kuzuhara, R. Tanibe, T. Kawai, T. Nakashima, Chirality induction in the synthesis of Ag₂₉ nanoclusters with asymmetric structure. J. Phys. Chem. C 125, 27009–27015 (2021).
- M. P. Moloney, J. Govan, A. Loudon, M. Mukhina, Y. K. Gun'ko, Preparation of chiral quantum dots. *Nat. Protoc.* 10, 558–573 (2015).
- Y. Li, T. Higaki, X. Du, R. Jin, Chirality and surface bonding correlation in atomically precise metal nanoclusters. Adv. Mater. 32, e1905488 (2020).
- P. T. Probst, S. Sekar, T. A. F. König, P. Formanek, G. Decher, A. Fery, M. Pauly, Highly oriented nanowire thin films with anisotropic optical properties driven by the simultaneous influence of surface templating and shear forces. ACS Appl. Mater. Interfaces 10, 3046–3057 (2018).
- H. Hu, S. Sekar, W. Wu, Y. Battie, V. Lemaire, O. Arteaga, L. V. Poulikakos, D. J. Norris, H. Giessen, G. Decher, M. Pauly, Nanoscale bouligand multilayers: Giant circular dichroism of helical assemblies of plasmonic 1D nano-objects. ACS Nano 15, 13653–13661 (2021).
- W. Ma, L. Xu, A. F. de Moura, X. Wu, H. Kuang, C. Xu, N. A. Kotov, Chiral inorganic nanostructures. Chem. Rev. 117, 8041–8093 (2017).
- J. Lu, Y. Xue, N. A. Kotov, Emerging trends in chiral inorganic nanostructures. *Israel J. Chem.* 61, 851–862 (2021).
- J. Lv, X. Gao, B. Han, Y. Zhu, K. Hou, Z. Tang, Self-assembled inorganic chiral superstructures. Nat. Rev. Chem. 6, 125–145 (2022).
- F. Li, F. Wu, X. Luan, Y. Yuan, L. Zhang, G. Xu, W. Niu, Highly enantioselective electrochemical sensing based on helicoid Au nanoparticles with intrinsic chirality. Sens. Actuators B 362, 131757 (2022).
- X.-F. Wu, Q. Ge, N. Jiang, M. Liu, H. Cong, Z. Tao, Ultrasensitive sensor for L-penicillamine with chirality-induced amplification of benzo[3]uril electrochemiluminescence via supramolecular interactions. Sens. Actuators B 362, 131801 (2022).
- M. Sun, Site-selective photoinduced cleavage and profiling of DNA by chiral semiconductor nanoparticles. Nat. Chem. 10, 821–830 (2018).
- D. E. Kharzeev, Y. Kikuchi, Real-time chiral dynamics from a digital quantum simulation. Phys. Rev. Res. 2, 023342 (2020).

SCIENCE ADVANCES | RESEARCH ARTICLE

- W. A. Gaviria Rojas, M. C. Hersam, Chirality-enriched carbon nanotubes for next-generation computing. Adv. Mater. 32, e1905654 (2020).
- 22. L. Daubersies, J.-B. Salmon, Evaporation of solutions and colloidal dispersions in confined droplets. *Phys. Rev. E* **84**, 031406 (2011).
- F. Clément, J. Leng, Evaporation of liquids and solutions in confined geometry. *Langmuir* 20. 6538–6541 (2004).
- C. B. Williamson, D. R. Nevers, A. Nelson, I. Hadar, U. Banin, T. Hanrath, R. D. Robinson, Chemically reversible isomerization of inorganic clusters. Science 363, 731–735 (2019).
- H. Han, S. Kallakuri, Y. Yao, C. B. Williamson, D. R. Nevers, B. H. Savitzky, R. S. Skye, M. Xu,
 O. Voznyy, J. Dshemuchadse, L. F. Kourkoutis, S. J. Weinstein, T. Hanrath, R. D. Robinson,
 Multiscale hierarchical structures from a nanocluster mesophase. *Nat. Mater.* 21,
 518–525 (2022)
- P. Navard, Formation of band textures in hydroxypropylcellulose liquid crystals. J. Polym. Sci. B 24, 435–442 (1986).
- J. Wang, S. Bhattacharya, M. M. Labes, Solvent evaporation induced torsad texture of sheared liquid-crystalline polymers. *Macromolecules* 24, 4942–4947 (1991).
- S. S. Patnaik, T. J. Bunning, W. W. Adams, J. Wang, M. M. Labes, Atomic force microscopy and high-resolution scanning electron microscopy study of the banded surface morphology of hydroxypropyl cellulose thin films. *Macromolecules* 28, 393–395 (1995).
- S. Chen, R. Qian, A study of band texture formation of nematic solutions of poly(1,4phenyleneterephthalamide) in sulfuric acid. *Die Makromolekulare Chemie* 191, 2475–2483 (1990)
- H. Zheng, W. Li, W. Li, X. Wang, Z. Tang, S. X. A. Zhang, Y. Xu, Uncovering the circular polarization potential of chiral photonic cellulose films for photonic applications. Adv. Mater. 30. e1705948 (2018).
- C. Langhammer, B. Kasemo, I. Zorić, Absorption and scattering of light by Pt, Pd, Ag, and Au nanodisks: Absolute cross sections and branching ratios. J. Chem. Phys. 126, 194702 (2007)
- Y. Yao, T. J. Ugras, T. Meyer, M. Dykes, D. Wang, A. Arbe, S. Bals, B. Kahr, R. D. Robinson, Extracting pure circular dichroism from hierarchically structured CdS magic cluster films. ACS Nano 16, 20457–20469 (2022).
- B. B. Patel, D. J. Walsh, D. H. Kim, J. Kwok, B. Lee, D. Guironnet, Y. Diao, Tunable structural color of bottlebrush block copolymers through direct-write 3D printing from solution. Sci. Adv. 6. eaaz7202 (2020).
- D. R. Nevers, C. B. Williamson, B. H. Savitzky, I. Hadar, U. Banin, L. F. Kourkoutis, T. Hanrath, R. D. Robinson, Mesophase formation stabilizes high-purity magic-sized clusters. *J. Am. Chem. Soc.* 140, 3652–3662 (2018).
- G. Albano, F. Salerno, L. Portus, W. Porzio, L. A. Aronica, L. di Bari, Outstanding chiroptical features of thin films of chiral oligothiophenes. *ChemNanoMat* 4, 1059–1070 (2018).
- J. W. Hovenier, Structure of a general pure Mueller matrix. Appl. Opt. 33, 8318–8324 (1994).
- W.-J. Chung, J. W. Oh, K. Kwak, B. Y. Lee, J. Meyer, E. Wang, A. Hexemer, S. W. Lee, Biomimetic self-templating supramolecular structures. *Nature* 478, 364–368 (2011).
- S. Jordens, L. Isa, I. Usov, R. Mezzenga, Non-equilibrium nature of two-dimensional isotropic and nematic coexistence in amyloid fibrils at liquid interfaces. *Nat. Commun.* 4, 1917 (2013).
- J. Wang, M. M. Labes, Control of the anisotropic mechanical properties of liquid crystal polymer films by variations in their banded texture. *Macromolecules* 25, 5790–5793 (1992).
- R. Bian, L. Meng, M. Zhang, L. Chen, H. Liu, Aligning one-dimensional nanomaterials by solution processes. ACS Omega 4, 1816–1823 (2019).
- Y. Yang, J. Liang, F. Pan, Z. Wang, J. Zhang, K. Amin, J. Fang, W. Zou, Y. Chen, X. Shi, Z. Wei, Macroscopic helical chirality and self-motion of hierarchical self-assemblies induced by enantiomeric small molecules. *Nat. Commun.* 9, 3808 (2018).
- 42. L. Yang, N. Su, J. Huang, X. Dou, C. Zhao, C. Feng, Chiral helical supramolecular hydrogels with adjustable pitch and diameter towards high-performance chiroptical detecting. *Giant* 8. 100077 (2021).
- R. Huang, S. H. Im, Dynamics of wrinkle growth and coarsening in stressed thin films. *Phys. Rev. E* 74, 026214 (2006).
- A. Guerrero-Martínez, B. Auguié, J. L. Alonso-Gómez, Z. Džolić, S. Gómez-Graña, M. Žinić, M. M. Cid, L. M. Liz-Marzán, Intense optical activity from three-dimensional chiral ordering of plasmonic nanoantennas. *Angew. Chem. Int. Ed.* 50, 5499–5503 (2011).
- W. C. Johnson Jr., Secondary structure of proteins through circular dichroism spectroscopy. Annu. Rev. Biophys. Biophys. Chem. 17, 145–166 (1988).
- P. Oswald, A. Dequidt, Lehmann effect in chiral liquid crystals and Langmuir monolayers: An experimental survey. *Liq. Cryst.* 36, 1071–1084 (2009).

- Y. Tsori, P. G. D. Gennes, Frustrated rotations in nematic monolayers. Eur. Phys. J. E Soft. Matter. 14. 91–96 (2004).
- X. He, J. Cheng, C. Patrick Collier, B. R. Srijanto, D. P. Briggs, Evaporation of squeezed water droplets between two parallel hydrophobic/superhydrophobic surfaces. *J. Colloid Interface* Sci. 576. 127–138 (2020).
- C. Chen, P. Duru, P. Joseph, S. Geoffroy, M. Prat, Control of evaporation by geometry in capillary structures. From confined pillar arrays in a gap radial gradient to phyllotaxy-inspired geometry. Sci. Rep. 7, 15110 (2017).
- C. B. Williamson, D. R. Nevers, T. Hanrath, R. D. Robinson, Prodigious effects of concentration intensification on nanoparticle synthesis: A high-quality, scalable approach. *J. Am. Chem. Soc.* 137, 15843–15851 (2015).
- A. Salij, R. H. Goldsmith, R. Tempelaar, Theory of apparent circular dichroism reveals the origin of inverted and noninverted chiroptical response under sample flipping. J. Am. Chem. Soc. 143, 21519–21531 (2021).
- W. B. Russel, D. A. Saville, W. R. Schowalter, Colloidal dispersions, in Cambridge Monographs on Mechanics (Cambridge Univ. Press. 2012).
- P. E. Cladis, J. T. Gleeson, P. L. Finn, H. R. Brand, Breathing mode in a pattern-forming system with two competing lengths. *Phys. Rev. Lett.* 67, 3239–3242 (1991).
- I. R. Bruss, G. M. Grason, Non-Euclidean geometry of twisted filament bundle packing. Proc. Natl. Acad. Sci. U.S.A. 109, 10781–10786 (2012).
- G. M. Grason, Braided bundles and compact coils: The structure and thermodynamics of hexagonally packed chiral filament assemblies. Phys. Rev. E 79, 041919 (2009).
- D. M. Hall, I. R. Bruss, J. R. Barone, G. M. Grason, Morphology selection via geometric frustration in chiral filament bundles. *Nat. Mater.* 15, 727–732 (2016).
- G. M. Grason, Chiral and achiral mechanisms of self-limiting assembly of twisted bundles. Soft Matter 16. 1102–1116 (2020).
- R. N. Kleiman, D. J. Bishop, R. Pindak, P. Taborek, Shear modulus and specific heat of the liquid-crystal blue phases. *Phys. Rev. Lett.* 53, 2137–2140 (1984).
- J. M. Ribó, J. Crusats, F. Sagués, J. Claret, R. Rubires, Chiral sign induction by vortices during the formation of mesophases in stirred solutions. Science 292, 2063–2066 (2001).
- D. K. Kondepudi, R. J. Kaufman, N. Singh, Chiral symmetry breaking in sodium chlorate crystallization. Science 250, 975–976 (1990).
- W. Dzwolak, Vortex-induced chiral bifurcation in aggregating insulin. Chirality 22, E154–E160 (2010).
- 62. T. M. Hermans, K. J. M. Bishop, P. S. Stewart, S. H. Davis, B. A. Grzybowski, Vortex flows impart chirality-specific lift forces. *Nat. Commun.* **6**, 5640 (2015).
- O. Lehmann, Structur, System und magnetisches Verhalten flüssiger Krystalle und deren Mischbarkeit mit festen. Ann. Phys. 307, 649–705 (1900).
- F. M. Leslie, Some thermal effects in cholesteric liquid crystals. Proc. R. Soc. London. Ser. A. Mathem. Phys. Sci. 307, 359–372 (1968).
- 65. P.-G. De Gennes, J. Prost, The physics of liquid crystals (Oxford Univ. Press, 1993).
- Y. Tabe, H. Yokoyama, Coherent collective precession of molecular rotors with chiral propellers. Nat. Mater. 2, 806–809 (2003).
- 67. D. Svenšek, H. Pleiner, H. R. Brand, Phase winding in chiral liquid crystalline monolayers due to lehmann effects. *Phys. Rev. Lett.* **96**, 140601 (2006).
- T. Shibata, A. S. Mikhailov, Nonequilibrium self-organization phenomena in active Langmuir monolayers. J. Nonlinear Sci. 16, 037108 (2006).
- T. Shibata, A. S. Mikhailov, Nonequilibrium pattern formation in chiral Langmuir monolayers with transmembrane flows. Europhys. Lett. 73, 436–442 (2006).
- S. Malola, H. Häkkinen, Chiral inversion of thiolate-protected gold nanoclusters via core reconstruction without breaking a Au–S Bond. J. Am. Chem. Soc. 141, 6006–6012 (2019).

Acknowledgments: We thank the following for invaluable discussions, B. Meijer, S. Meskers, N. Abbott, P.-T. Brun, G. Grason, R. Huang, R. Robinson, and S. Weinstein. Funding: This work was primarily supported by the National Science Foundation (NSF) as a seed grant in the Cornell Center of Materials Research (CCMR) NSF MRSEC program (DMR-1719875) and the REU program DMR-1757420. Author contributions: Conceptualization: T.H. and A.V.G. Methodology: T.H. and A.V.G. Investigation: T.H., A.V.G., and M.G. Visualization: T.H. and A.V.G. Supervision: T.H. Writing—original draft: T.H. and A.V.G. Writing—review and editing: T.H. and A.V.G. Competing interests: The authors declare that they have no competing interests. Data and materials availability: All data needed to evaluate the conclusions in the paper are present in the paper and/or the Supplementary Materials.

Submitted 4 May 2023 Accepted 6 October 2023 Published 8 November 2023 10.1126/sciadv.adi5520

Downloaded from https://www.science.org at Cornell University on December 07, 2022

Science Advances

Emergence and inversion of chirality in hierarchical assemblies of CdS nanocrystal fibers

Alexander V. Gonzalez, Miranda Gonzalez, and Tobias Hanrath

Sci. Adv. 9 (45), eadi5520. DOI: 10.1126/sciadv.adi5520

View the article online

https://www.science.org/doi/10.1126/sciadv.adi5520 **Permissions**

https://www.science.org/help/reprints-and-permissions

Use of this article is subject to the Terms of service